# Electronic Supplementary Information

## "Pit-dot" ultrathin nanosheets of hydrated copper pyrophosphate as efficient pre-catalysts for robust water oxidation

Junfeng Xie,[†,*] Xueying Yang,[†] Yameng Wang, Luyao Kang, Jiechen Li, Zimeng Wei, Pin Hao, Fengcai Lei, Qian Wang, Bo Tang[*]

College of Chemistry, Chemical Engineering and Materials Science, Key Laboratory of Molecular and Nano Probes (Ministry of Education), Collaborative Innovation Center of Functionalized Probes for Chemical Imaging in Universities of Shandong, Institute of Molecular and Nano Science, Shandong Normal University, Jinan, Shandong, 250014, P. R. China. E-mail: xiejf@sdnu.edu.cn; tangb@sdnu.edu.cn.

† These authors contributed equally to this work.

# 1. Experimental Section

## 1.1 Materials

The chemicals were purchased from Sinopharm Chemical Reagent Co., Ltd. and used as received without further purification.

## 1.2 Preparation of the $Cu(OH)_2$ nanoarrays (CH) grown on copper foam

The copper foam (CF) was cut into pieces with size of 1 cm × 1.5 cm, then ultrasonically cleaned in an acetone solution for 5 min to remove the surface organics, rinsed in 1% HCl solution to remove the oxide layer on the surface, and washed with deionized water. After that, anodic oxidation was conducted on an electrochemical setup. In detail, a piece of CF was served as the working electrode, a platinum gauze was selected as the counter electrode, an Hg/HgO electrode was used as the reference electrode, and 3 M KOH solution was used as the electrolyte. The anodic current density was set as 30 mA $cm^{-2}$, and the duration time was 800 s. After that, the as-obtained $Cu(OH)_2$ nanoarrays (CH) was washed with deionized water and ethanol for several times, and dried overnight under vacuum.

## 1.3 Synthesis of the $Cu_2P_2O_7{\cdot}3H_2O$ "pit-dot" ultrathin nanosheets (CPO-PDNS) and the $Cu_2P_2O_7{\cdot}3H_2O/Cu(OH)_2$ intermediate (CPO/CH)

For the synthesis of the hydrated copper pyrophosphate "pit-dot" ultrathin nanosheets grown on copper foam (CPO-PDNS), 0.4 mmol $K_2HPO_4{\cdot}3H_2O$ was firstly dissolved in 30 mL deionized water, and the pH value of solution was adjusted to 4 using 3 M $H_3PO_4$ solution. Then, the as-prepared CH was placed into the solution and maintained still at room temperature for 3 hours. The product was then washed with deionized water and ethanol for several times, and dried overnight under vacuum. By simply shortening the reaction period to 1 hour, the CPO/CH intermediate with co-presence of $Cu_2P_2O_7{\cdot}3H_2O$ and $Cu(OH)_2$ can be prepared.

## 1.4 Structural characterizations

The X-ray diffraction (XRD) was performed on a Philips X'Pert Pro Super diffractometer with Cu Kα radiation (λ=1.54178 Å). The scanning electron

microscopy (SEM) images were taken on a JEOL JSM-6700F SEM. The transmission electron microscopy (TEM) was carried out on a JEM-2100F field emission electron microscope at an acceleration voltage of 200 kV. The high-resolution TEM (HRTEM), selected area electron diffraction (SAED), high-angle annular dark-field scanning transmission electron microscopy (HAADF-STEM) and corresponding elemental mapping analyses were performed on a Thermo Fischer Talos F200X TEM. The X-ray photoelectron spectroscopy (XPS) analyses were performed on a VGESCALAB MKII X-ray photoelectron spectrometer with an excitation source of Mg Kα=1253.6 eV, and the resolution level was lower than 1 atom%. The Raman spectroscopy was performed with a laser micro-Raman spectrometer (Horiba LabRAM HR Evolution, 532 nm excitation wavelength).

**1.5 Electrocatalytic study**

All the electrochemical measurements were performed in a three-electrode system linked with an electrochemical workstation (Ivium Vertex. C. EIS). All potentials were calibrated to a reversible hydrogen electrode (RHE) according to the Nernst equation and the data were presented without iR correction. An Hg/HgO electrode was used as the reference electrode, a platinum gauze electrode (2 cm × 2 cm, 60 mesh) was used as the counter electrode, and the CF-supported catalyst was served as the working electrodes which was fixed with an electrode holder connected by a glassy carbon plate. The linear sweeping voltammetry (LSV) tests were conducted at a scan rate of 2 mV $s^{-1}$ in the electrolytes of $O_2$-purged 1 M KOH solution, and the electrochemical impedance spectroscopy (EIS) data were acquired in the same configuration at 1.6 V vs. RHE from $10^{-2}$-$10^5$ Hz.

## 2. Method for the identification of the crystal facets

The identification of the crystal facets in the HRTEM image in Fig. 1E was performed by means of the calculation from the crystallographic formulae for interplanar angles for monoclinic system as

$$\cos\phi = \frac{d_1 d_2}{\sin^2\beta}\left[\frac{h_1 h_2}{a^2} + \frac{k_1 k_2 \sin^2\beta}{b^2} + \frac{l_1 l_2}{c^2} - \frac{(l_1 h_2 + l_2 h_1)\cos\beta}{ac}\right]$$

where the ($h_1$, $k_1$, $l_1$) and ($h_2$, $k_2$, $l_2$) correspond to the possible crystal plane index, and the parameters of a, b, c and β are the cell parameters of the monoclinic $Cu_2P_2O_7 \cdot 3H_2O$ lattice. When potential combinations of facets with proper interplanar spacing were imported into the crystallographic formulae, the interplanar angles $\Phi$ between the proposed facets can be obtained. When the resulted interplanar angle $\Phi$ matches the angle measured from the HRTEM image, the combination of facets is correct. In this work, a series of combinations of facets were imported into the crystallographic formulae, and an interplanar angle Φ of 65.4° was obtained when the (033) and (420) planes were imported. The as-obtained angle matches well with the measured value, therefore confirming the crystal facets of (033) and (420) planes in the HRTEM image.

## 3. Additional physical and electrochemical characterizations

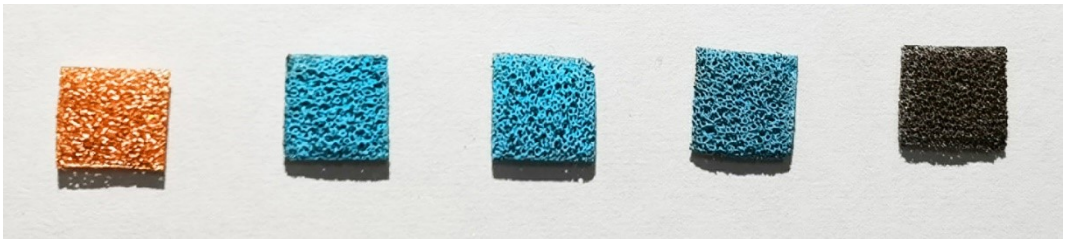

**Fig. S1** Photograph of the samples. From left to right: CF, CH, CPO/CH, CPO-PDNS and CPO-PDNS-pc.

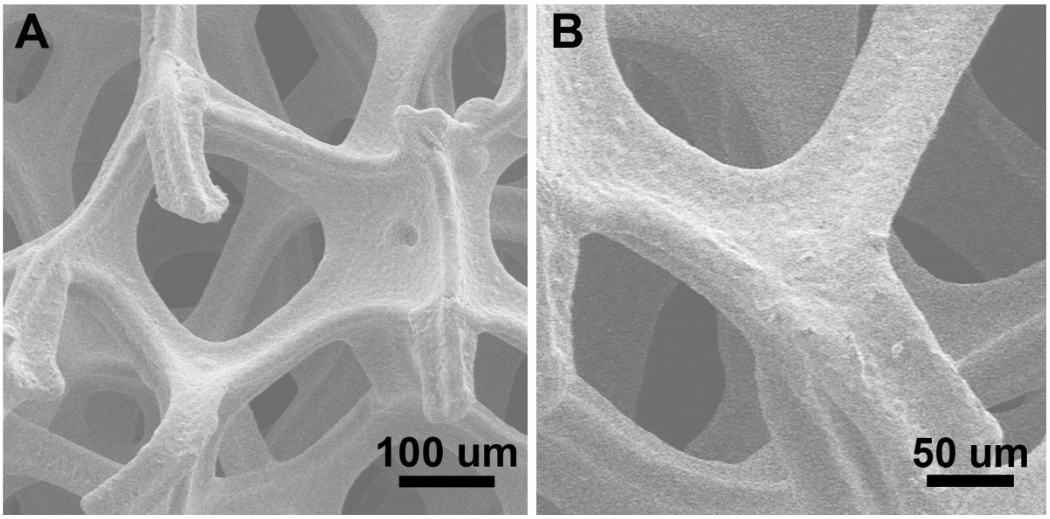


**Fig. S2** (A-B) SEM images of the bare copper foam.

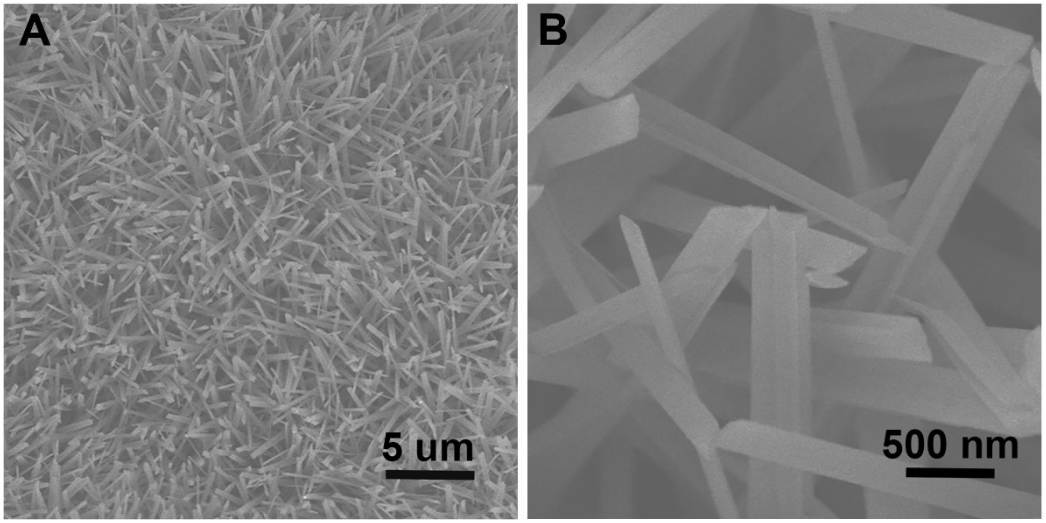


**Fig. S3** (A-B) SEM images of the $Cu(OH)_2$ nanoarrays grown on copper foam (CH).

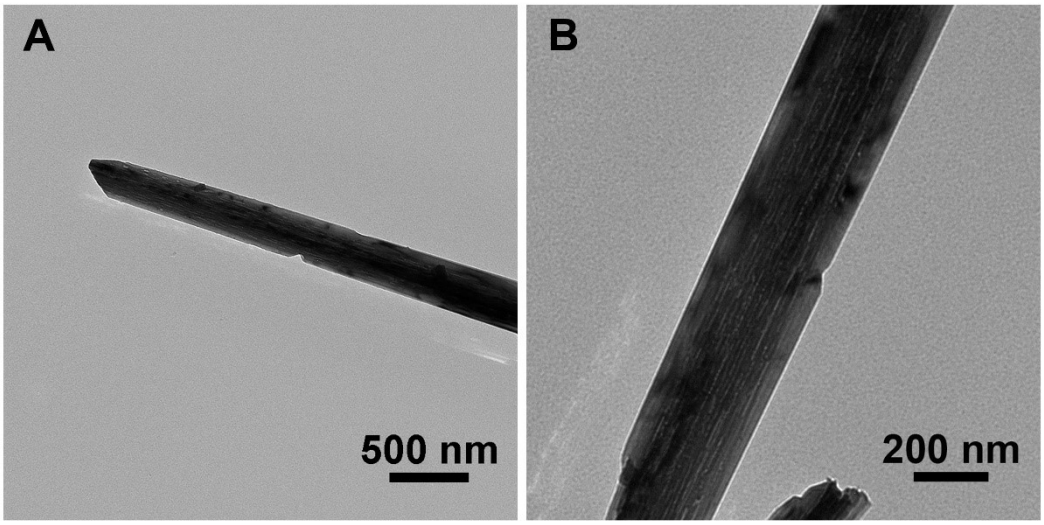


**Fig. S4** (A-B) TEM images of CH.

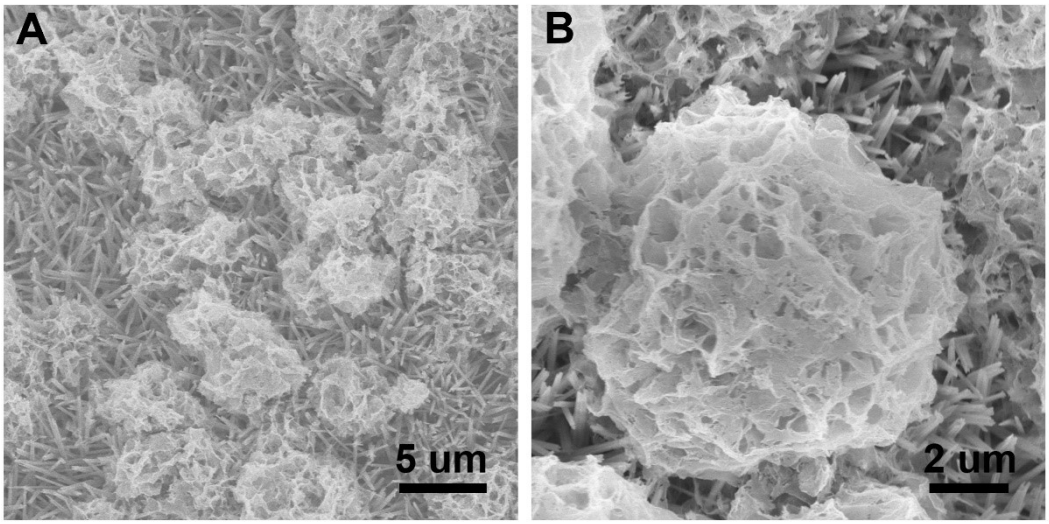


**Fig. S5** (A-B) SEM images of the $Cu_2P_2O_7 \cdot 3H_2O/Cu(OH)_2$ intermediate (CPO/CH). The co-presence of $Cu_2P_2O_7 \cdot 3H_2O$ nanosheets and $Cu(OH)_2$ nanowires can be seen.

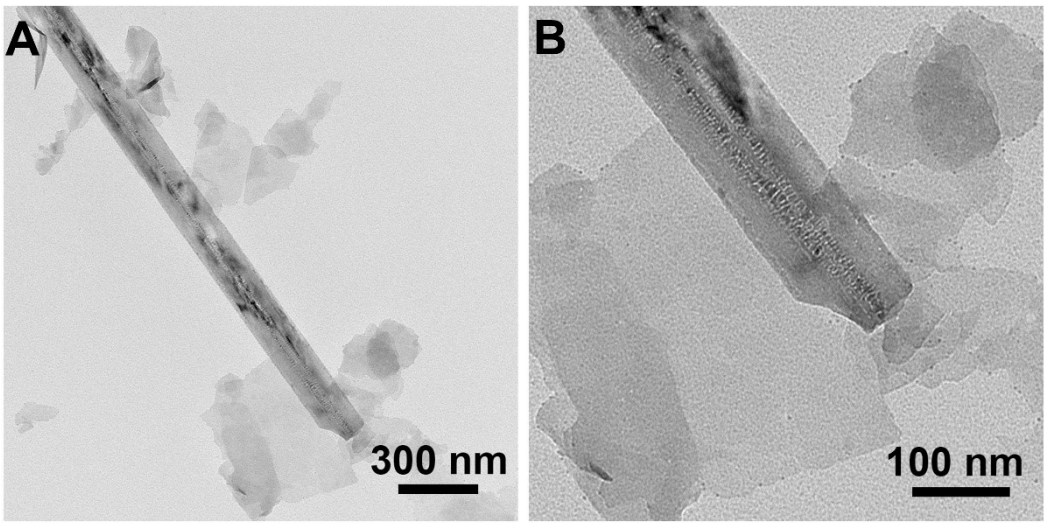


**Fig. S6** (A-B) TEM images of CPO/CH.

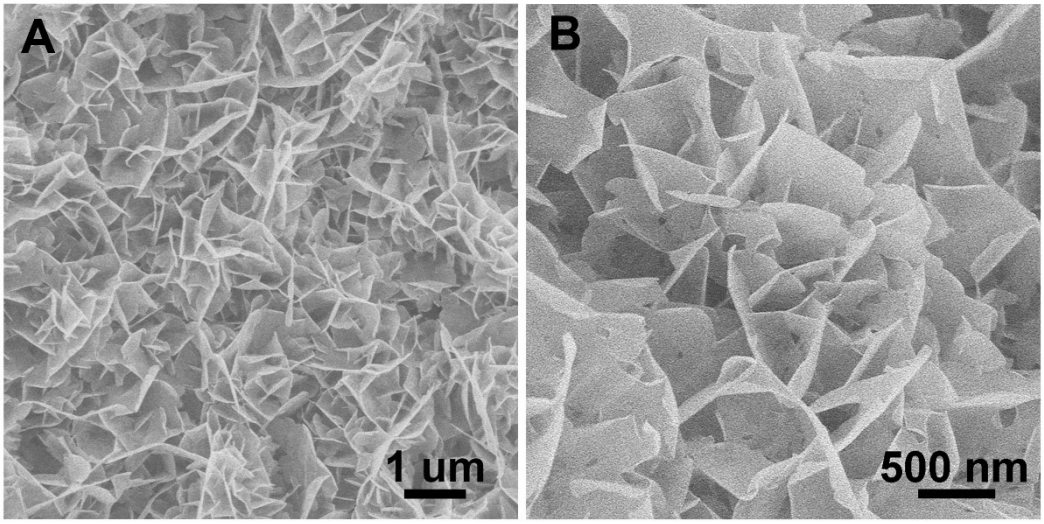


**Fig. S7** (A-B) SEM images of the $Cu_2P_2O_7 \cdot 3H_2O$ "pit-dot" ultrathin nanosheets (CPO-PDNS).

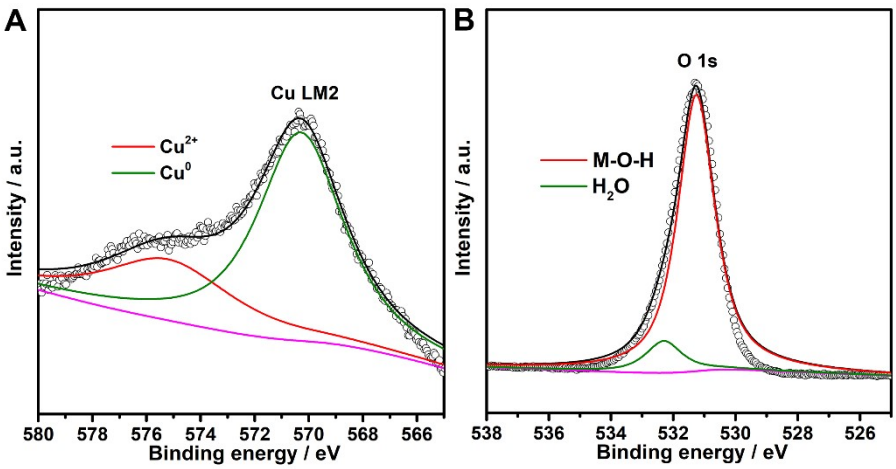


**Fig. S8** (A) Auger electron spectrum of Cu in CH. (B) XPS O 1s spectrum of CH.

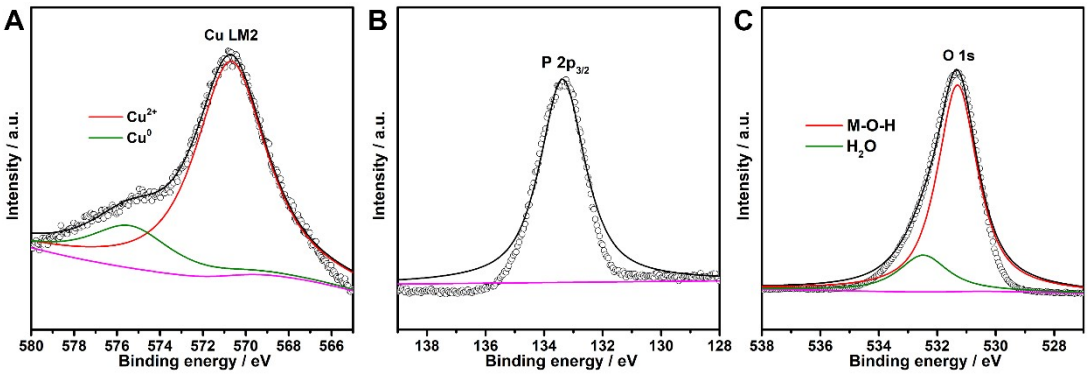


**Fig. S9** (A) Auger electron spectrum of Cu in CPO/CH. (B) XPS P 2p spectrum and (C) XPS O 1s spectrum of CPO/CH.

**Table S1** Comparison of the OER performance of different catalysts.

| | η@10 mA $cm^{-2}$ [mV] | $j_{geo}$@1.7 V vs. RHE [mA $cm^{-2}$] | activity retention @operation time | Reference |
|---|---|---|---|---|
| CF | 474 | 9.1 | / | this work |
| CH | 354 | 21.0 | / | this work |
| CPO/CH | 262 | 33.2 | / | this work |
| CPO-PDNS | 195 | 91.2 | 260%@720h | this work |
| CPO-PDNS-pc | 97* | 158.2 | / | this work |
| CuFe PBA/CH/CF | 193 | 103.8 | 234%@300h | 1 |
| $Cu_2S$/CF | 270 | 47 | 101%@24h | 2 |
| $Cu_2O$/CF | 350 | 117 | 100%@50h | 3 |
| $Cu_2Se$/CF | 320 | 50 | 90%@6h | 4 |
| CuO/$Cu_2O$/CF | 290 | 84 | 100%@50h | 5 |
| Cu-$RuO_2$ | 191 | / | 108%@8h | 6 |
| CuO-TCNQ/CF | 280 | / | 93%@24h | 7 |
| $Cu_2O_xS_{1-x}$ | 330 | 130 | 100%@3.3h | 8 |
| CuO nanosheets | 350 | 65 | 79%@8h | 9 |
| $Co_{0.3}CuO_x$/NF | 290 | 45 | 100%@26h | 10 |
| $Cu_3P$/FeP | 315 | / | 106%@50h | 11 |
| $Cu_3P$ | 553 | 4 | / | 11 |
| FeP | 398 | 42 | / | 11 |
| $Ni_2P_2O_7 \cdot 8H_2O$ | 239 | / | 120%@9h | 12 |
| $(Fe_4Co)P_2O_7$@N–C | 341 | / | 109%@80h | 13 |
| $Fe_2P_2O_7$@N–C | 490 | 8 | / | 13 |
| $(Fe_{12}Co)P_2O_7$@N–C | 425 | 47 | / | 13 |
| $(Fe_3Co)P_2O_7$@N–C | 370 | 45 | / | 13 |
| Co-Pi-8W | 383 | 144 | / | 14 |
| Co-Pi-4W | 281 | 47 | 120%@72h | 14 |
| Co-Pi-2W | 359 | 85 | / | 14 |
| Co-Pi | 254 | 58 | / | 14 |
| $Co_3(PO_4)_2$ | 340 | 100 | / | 15 |
| $NiCo_2(PO_4)_2$ | 365 | 20 | / | 15 |
| $CoNi_2(PO_4)_2$ | 405 | 80 | 87%@2h | 15 |
| $NaCo_4(PO_4)_3$ | 550 | 5 | 99%@10h | 16 |
| $Na_2Co_2P_2O_7$ | 570 | 2.5 | / | 16 |
| $Co_2P_2O_7$@C | 397 | 32 | 82%@22h | 17 |
| $Co_2P_2O_7$ | 490 | 8 | / | 17 |
| $Co(PO_3)_2$ | 574 | 4 | / | 17 |

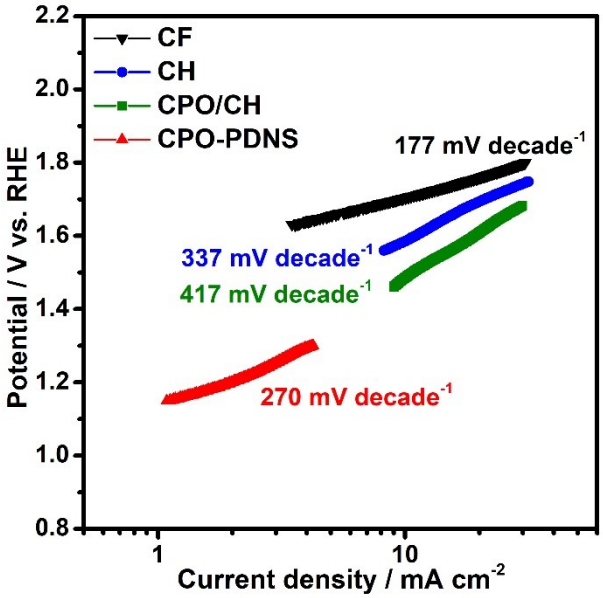


**Fig. S10** The Tafel plots of the Cu-based catalysts.

As shown in Fig. S10, the bare copper foam (CF) exhibits lower Tafel slope of 177 mV decade$^{-1}$. For the Cu-based catalysts with surface active layers, large Tafel slopes can be resulted. In detail, CPO-PDNS shows lower Tafel slope of 270 mV decade$^{-1}$ than that of CH (337 mV decade$^{-1}$) and CPO/CH (417 mV decade$^{-1}$). However, owing to the simultaneous occurrence of the pre-oxidation reaction and the OER process, the Tafel slopes cannot be used for evaluating the reaction kinetics of OER catalysis.

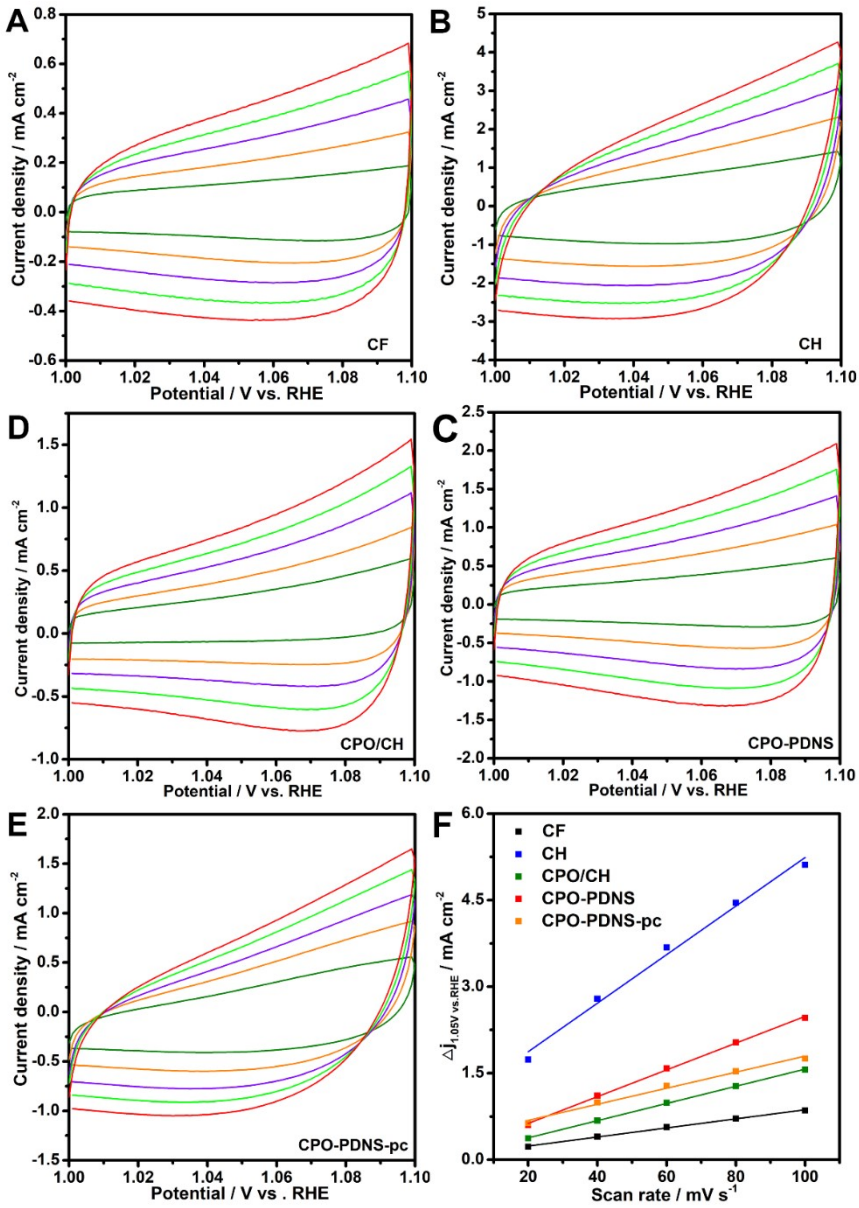


**Fig. S11** (A-E) CV curves in the non-redox region for the estimation of $C_{dl}$ values of CF, CH, CPO/CH, CPO-PDNS and CPO-PDNS-pc. (F) The estimation of $C_{dl}$ values by plotting the $\Delta j$ ($j_{anodic}$-$j_{cathodic}$) at 1.05 V vs. RHE against the scan rate.

The estimation of the effective active surface area was carried out according to literatures.[18, 19] As shown in Fig. S11A-E, the cyclic voltammetry (CV) measurements were conducted at various scan rates (20, 40, 60, 80, 100 mV $s^{-1}$) in the non-redox region of 1.0-1.1 V vs. RHE, which can be considered as the double-layer capacitive behavior. The electrochemical double-layer capacitance ($C_{dl}$) of the catalysts can be calculated from the CV curves, which is linearly proportional to the electrochemically

active surface area. As revealed in Fig. S11F, the $C_{dl}$ value is estimated by plotting the $\Delta j$ ($j_{anodic}$-$j_{cathodic}$) at 1.05 V vs. RHE against the scan rate, where the slope is twice $C_{dl}$. The calculated $C_{dl}$ values were listed in Table 1.

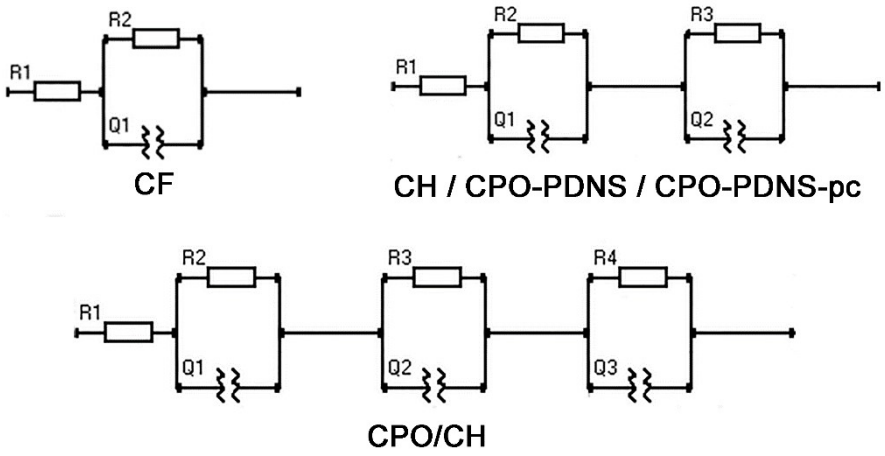


**Fig. S12** The equivalent circuits of various catalysts for fitting the electrochemical impedance spectra (EIS).

The electrochemical impedance spectra (EIS) data plotted in Fig. 3C can be fitted according to various equivalent circuits as shown in Fig. S12. Typically, three basic elements can be observed for all the tested samples, where $R_1$ and $R_2$ represent the series resistance ($R_s$) and charge-transfer resistance ($R_{ct}$), and $Q_1$ corresponds to the solid-electrolyte interfacial capacitance, respectively. Besides, two additional elements, i.e., $R_3$ and $Q_2$, can be identified for CH, CPO-PDNS and CPO-PDNS-pc, which represent the interface resistance ($R_{int}$) and Faradaic capacitance derived from the solid-electrolyte interface process, and the solid refers to $Cu(OH)_2$, $Cu_2P_2O_7{\cdot}3H_2O$ and CuO, respectively. In addition, a more complex equivalent circuit was used for fitting the EIS data of CPO/CH, where $R_3$/$R_4$ and $Q_2$/$Q_3$ correspond to the $R_{int}$ values and Faradaic capacitances derived from the co-existed $Cu(OH)_2$/electrolyte and $Cu_2P_2O_7{\cdot}3H_2O$/electrolyte interfaces, respectively.[20]

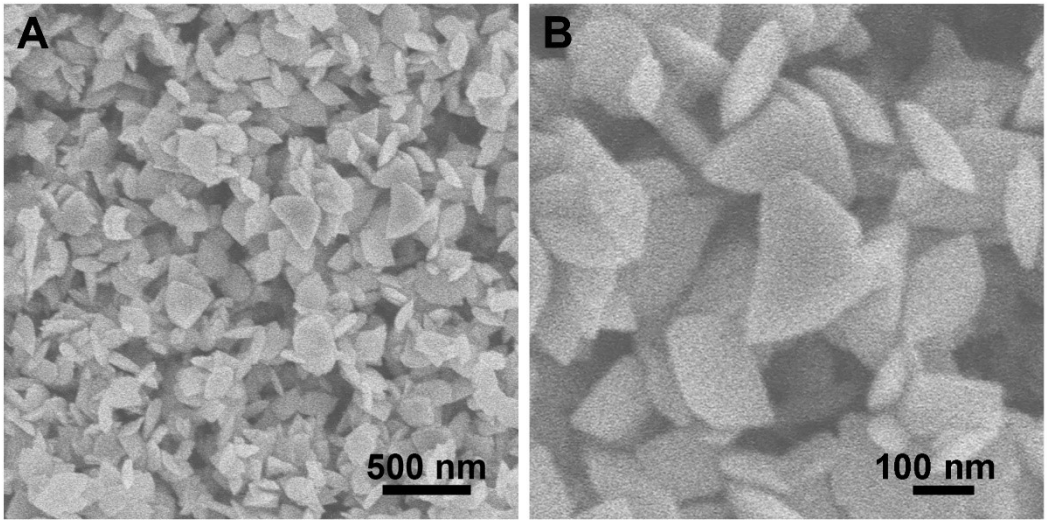


**Fig. S13** (A-B) SEM images of CPO-PDNS-pc.

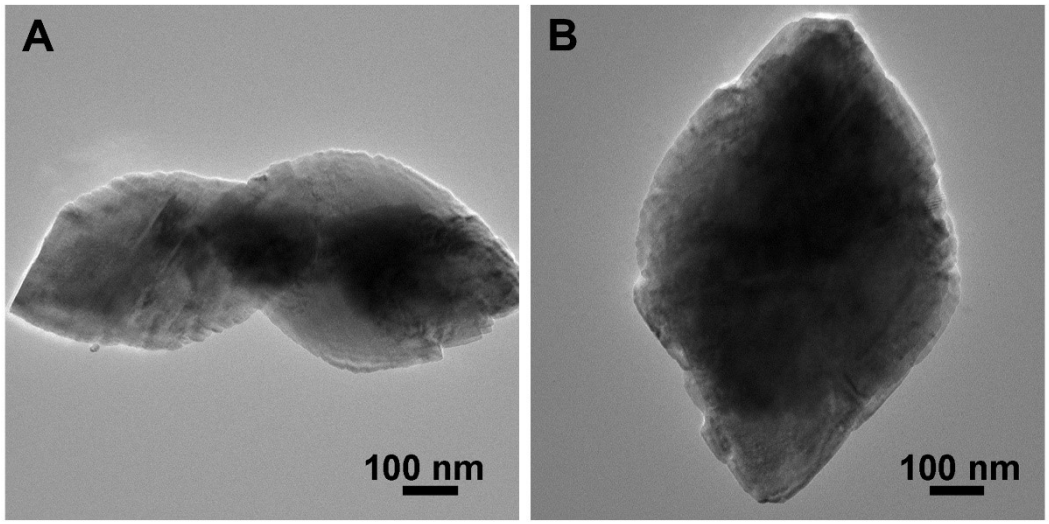


**Fig. S14** (A-B) Additional TEM images of CPO-PDNS-pc.

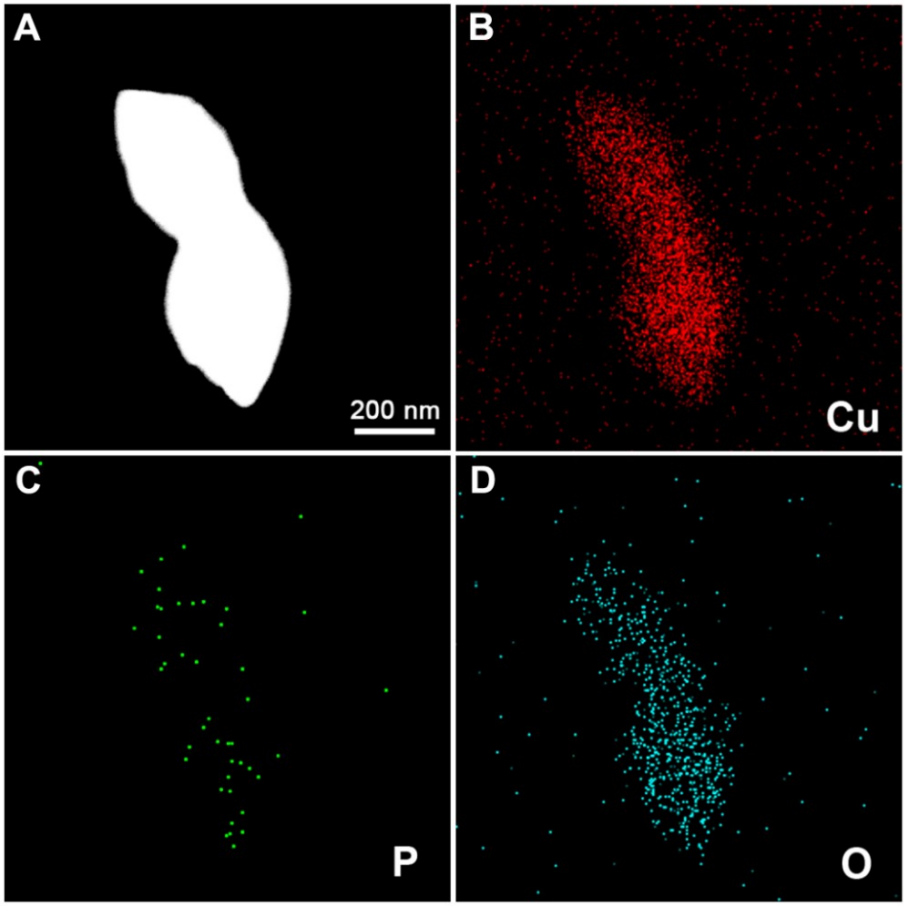


**Fig. S15** (A-D) HAADF-STEM image and the corresponding elemental mapping analyses of CPO-PDNS-pc.

**Table S2** The variation of relative contents of elements during the stability test. As can be seen, the content of P undergoes obvious decrement as the OER operation proceeds.

| | Cu | P | O |
|---|---|---|---|
| CPO-PDNS | 1.000 | 0.963 | 4.052 |
| CPO-PDNS-15min | 1.000 | 0.200 | 3.693 |
| CPO-PDNS-pc | 1.000 | 0.004 | 2.000 |

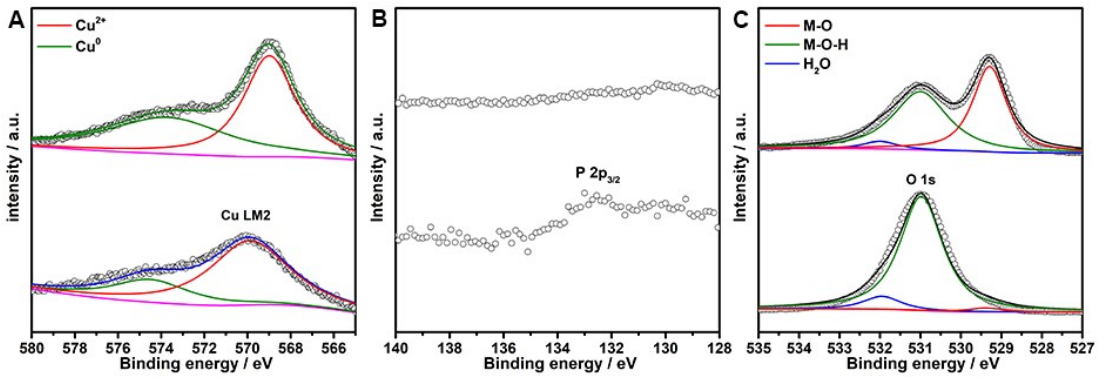


**Fig. S16** AES and XPS spectra of CPO-PDNS after 15-min (bottom) and 30-day (top) OER catalysis. (A) AES Cu LM2 spectra. (B-C) XPS P 2p and O 1s spectra.

The AES Cu and XPS O spectra of the CPO-PDNS pre-catalyst after 15-min and 30-day OER catalysis were plotted in Fig. S16. As can be seen from Fig. S16A, the dominance of $Cu^{2+}$ species can be confirmed for both CPO-PDNS-15min and CPO-PDNS-pc. In addition, Fig. S16B clearly reveals the weak signal of P owing to the irreversible phase transformation from $Cu_2P_2O_7 \cdot 3H_2O$ to CuO, which is consistent with the result from XRD analyses. Besides, the O 1s spectra in Fig. S16C reveal the dominance of the -OH species binding with the metal ions for CPO-PDNS-15min, while the emergence of the deconvoluted peak of M-O bonds for CPO-PDNS-pc after 30-day OER operation indicates the generation and accumulation of the active CuO phase during the long-term catalysis, which agrees well with the results from XRD and HRTEM analyses.

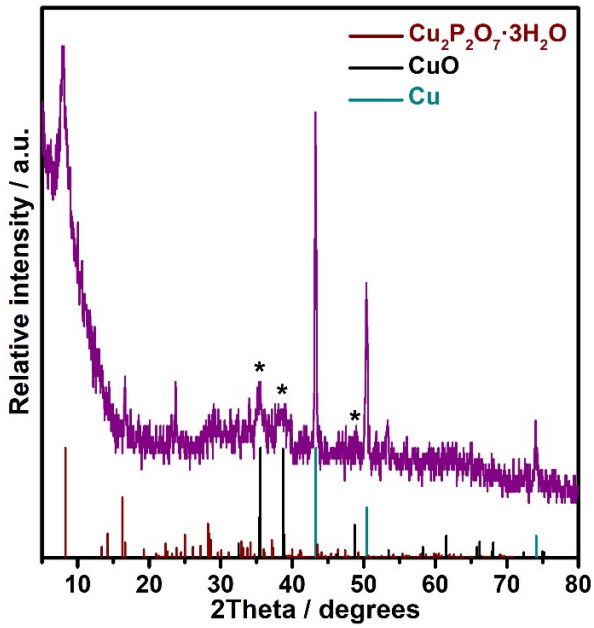


**Fig. S17** XRD pattern of CPO-PDNS after 15-min OER catalysis. CuO phase could be detected after 15-min OER operation, suggesting the fast phase transformation from $Cu_2P_2O_7 \cdot 3H_2O$ to the catalytically active CuO species.

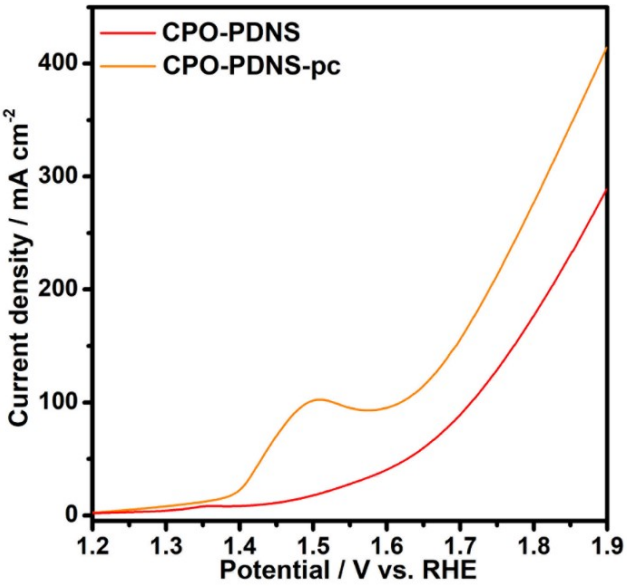


**Fig. S18** LSV curves of the CPO-PDNS pre-catalyst before and after 30-day OER catalysis.

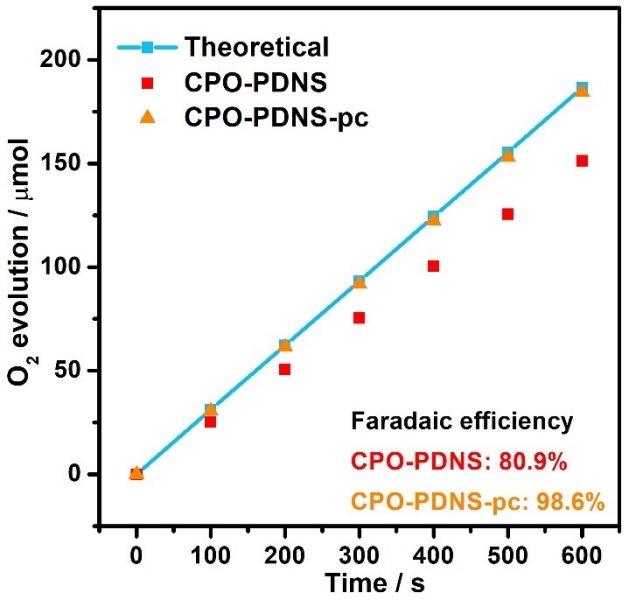


**Fig. S19** The calculated Faradaic efficiency of CPO-PDNS and CPO-PDNS-pc.

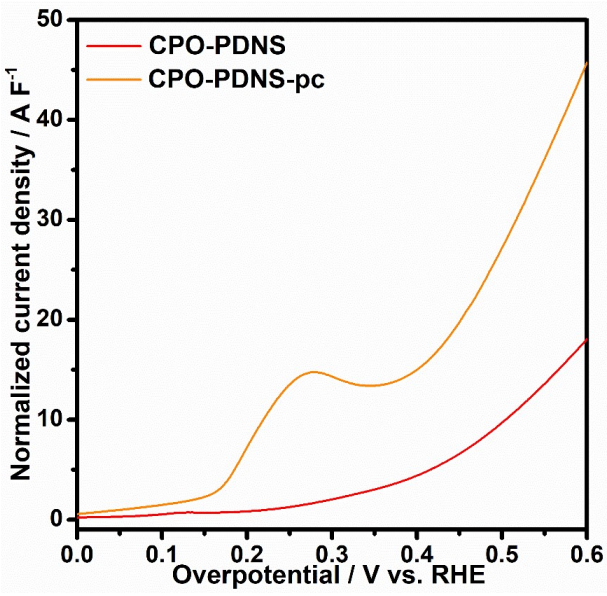


**Fig. S20** $C_{dl}$-normalized LSV curves of the CPO-PDNS pre-catalyst before and after 30-day OER catalysis.

## Reference

1. X. Yang, L. Kang, Z. Wei, S. Lou, F. Lei, P. Hao, J. Xie and B. Tang, *Chem. Eng. J.*, 2021, **422**, 130139.
2. S. B. Kale, P. T. Babar, J.-H. Kim and C. D. Lokhande, *New J. Chem.*, 2020, **44**, 8771-8777.

3. H. Xu, J.-X. Feng, Y.-X. Tong and G.-R. Li, *ACS Catal.*, 2017, **7**, 986-991.
4. J. Masud, W. P. R. Liyanage, X. Cao, A. Saxena and M. Nath, *ACS Appl. Energy Mater.*, 2018, **1**, 4075-4083.
5. T. N. Huan, G. Rousse, S. Zanna, I. T. Lucas, X. Xu, N. Menguy, V. Mougel and M. Fontecave, *Angew. Chem. Int. Ed.*, 2017, **56**, 4792-4796.
6. J. Su, R. Ge, K. Jiang, Y. Dong, F. Hao, Z. Tian, G. Chen and L. Chen, *Adv. Mater.*, 2018, **30**, 1801351.
7. X. Ren, X. Ji, Y. Wei, D. Wu, Y. Zhang, M. Ma, Z. Liu, A. M. Asiri, Q. Wei and X. Sun, *Chem. Commun.*, 2018, **54**, 1425-1428.
8. X. Zhang, X. Cui, Y. Sun, K. Qi, Z. Jin, S. Wei, W. Li, L. Zhang and W. Zheng, *ACS Appl. Mater. Interfaces*, 2018, **10**, 745-752.
9. S. M. Pawar, B. S. Pawar, B. Hou, J. Kim, A. T. Aqueel Ahmed, H. S. Chavan, Y. Jo, S. Cho, A. I. Inamdar, J. L. Gunjakar, H. Kim, S. Cha and H. Im, *J. Mater. Chem. A*, 2017, **5**, 12747-12751.
10. W. Niu, J. Shi, L. Ju, Z. Li, N. Orlovskaya, Y. Liu and Y. Yang, *ACS Catal.*, 2018, **8**, 12030-12040.
11. H. Kim, K. Min, C. Lim, S. E. Shim, D. Lim and S.-H. Baeck, *Int. J. Hydrogen Energy*, 2021, **46**, 32364-32372.
12. S. J. Marje, P. K. Katkar, S. B. Kale, A. C. Lokhande, C. D. Lokhande and U. M. Patil, *J. Alloy. Compd.*, 2019, **779**, 49-58.
13. D. Zhao, Q. Shao, Y. Zhang and X. Huang, *Nanoscale*, 2018, **10**, 22787-22791.
14. J. Qi, J. Xie, Z. Wei, S. Lou, P. Hao, F. Lei and B. Tang, *Chem. Commun.*, 2020, **56**, 4575-4578.
15. J. Zhang, Y. Yang, Z. Zhang, X. Xu and X. Wang, *J. Mater. Chem. A*, 2014, **2**, 20182-20188.
16. H. Wan, R. Ma, X. Liu, J. Pan, H. Wang, S. Liang, G. Qiu and T. Sasaki, *ACS Energy Lett.*, 2018, **3**, 1254-1260.
17. Y. Chang, N.-E. Shi, S. Zhao, D. Xu, C. Liu, Y.-J. Tang, Z. Dai, Y.-Q. Lan, M. Han and J. Bao, *ACS Appl. Mater. Interfaces*, 2016, **8**, 22534-22544.
18. M. A. Lukowski, A. S. Daniel, F. Meng, A. Forticaux, L. Li and S. Jin, *J. Am. Chem. Soc.*, 2013, **135**, 10274-10277.
19. J. Xie, J. Zhang, S. Li, F. Grote, X. Zhang, H. Zhang, R. Wang, Y. Lei, B. Pan and Y. Xie, *J. Am. Chem. Soc.*, 2013, **135**, 17881-17888.
20. D. U. Lee, H. W. Park, M. G. Park, V. Ismayilov and Z. Chen, *ACS Appl. Mater. Interfaces*, 2015, **7**, 902-910.